

## Chapter 2

# Joint least-squares inversion of up- and down-going signal for ocean bottom data sets

This chapter presents a joint least-squares inversion method for imaging the acoustic primary (up-going) and mirror (down-going) signals for ocean-bottom seismic (OBS) processing. Joint inversion combines into one image the benefits of wider illumination from the mirror signal and wider angular illumination from the primary signal into one image. Results from a synthetic SEAM model and the 2D Cascadia ocean-bottom node field dataset show better subsurface illumination and improved resolution in geologically complex areas.

Ocean-bottom seismic acquisition is an established technology in which seismometers are placed at the sea-bottom and shots are fired at the sea surface. In areas congested by platforms or other obstacles, OBS acquisition is advantageous because it is operated by small boats without cumbersome towed streamers. Such a geometry enables OBS acquisition to provide full-azimuth illumination, shear-wave recording, a quiet recording environment, high-resolution data and repeatability. Applications of OBS acquisition includes imaging in obstructed oilfields and time-lapse monitoring

of hydrocarbon reservoirs.

There are different processing schemes for ocean bottom data. The traditional way, inherited from surface seismic processing, is to remove all free-surface multiples and to migrate only with the primary signal (Wang et al., 2009). Therefore, initial work on OBS data processing has been dedicated to the removal of free-surface multiples. One way to attenuate strong free-surface multiples is to combine the geophone and hydrophone recordings to eliminate the receiver ghost and the water column reverberations, a technique known as PZ summation (Barr and Sander, 1989; Soubaras, 1996; Schalkwijk et al., 2003). The vertical component of the geophone (Z) records up- and down-going signal at opposite polarity. The hydrophone recording (P) is not sensitive to whether the energy is coming from above or below. In this way, we can separate out the up- and down-going signal by adding and subtracting the P and Z recording in OBN data. As an alternative to PZ summation, Sonneland and Berg (1987) and Amundsen (2001) addressed free-surface multiples with the theory of up-down deconvolution in both layered and complex media. In this approach, not only are all free-surface multiples attenuated, but also de-ghosting and signature deconvolution are conducted in a single step.

Although multiples are often treated as noise, they are formed by the same source signal as primaries but travel along different paths in the medium. The receiver ghost, also known as the mirror signal, is the next order of reflection beyond the primaries. The receiver ghost has an additional reflection off the sea surface. The source grid in a deep water OBS survey has a much wider lateral extent than the receiver grid. Therefore, the subsurface reflection point of the receiver ghost is located at greater distances from the receiver station than the primaries (Figure 2.1). The mirror signal can provide wider subsurface illumination than the primaries if the energy is properly migrated. Several authors have used the mirror signal in the migration of OBS data (Godfrey et al., 1998; Ronen et al., 2005; Grion et al., 2007; Dash et al., 2009).

While most authors conclude that the mirror image produces a better result than the conventional primary image, the information in the primary image is also valuable. The primary reflection can illuminate the subsurface at a different reflection angle

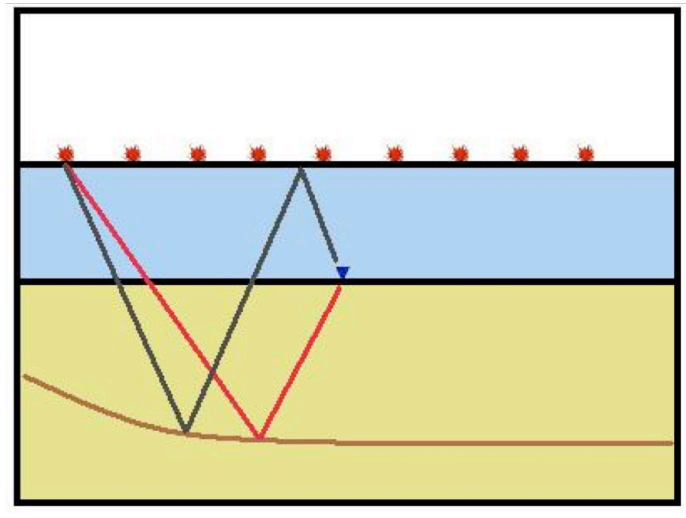


Figure 2.1: The subsurface reflection point of the receiver ghost, also known as the mirror signal (in black), is located at a greater distance from the receiver station than the primary signal (in red). For a deep water OBS survey, the source grid has a much wider lateral extent than the receiver grid. This translates to a wider subsurface illumination for the mirror signal than the primaries, and it provides more potential for velocity and AVO analysis. [NR] chap2/. illum

than the mirror reflection (Figure 2.2). Figure 2.2 shows the illumination angle by two of the ocean bottom receivers with primary and mirror reflection. Theoretically, if there is an acquisition geometry with a dense sampling of sources and receivers and at a very large lateral extend, we can expect the subsurface image point to be illuminated by a wide and continuous range of angles. However, in the ocean bottom node acquisition, the receiver grid is often sparse. This means that the subsurface angular illumination can be very different between different order of reflections.

The Kirchhoff migration result from Dash et al. (2009) highlights the difference between the two types of signals. The illumination area from the mirror signal is much wider than the illumination area from the primary signal (Figure 2.3). However, as annotated by the circled region (Figure 2.3), the primary contains more details than the mirror image. Figure 2.4 shows six rays with the same source and receiver pairs illuminating the subsurface with the primary reflection (Figure 2.4a) and the mirror reflection (Figure 2.4b). The image point of each ray is shown in the yellow region. The primary reflection image point is much closer together than the mirror reflection image point. Although the mirror signal can image a bigger area, the primary signal has a higher image space sampling. Instead of treating the primary image and the mirror image separately, I can combine the information from the two sets of data coherently by joint least-squares reverse-time migration (LSRTM). The LSRTM imaging method can improve the structure and aperture of the seismic images by using both the up-going primary and the down-going mirror signals.

Muijs et al. (2007b) made an early attempt to image primary and free-surface multiples together. It requires the data to be decomposed into up-going and down-going constituents at the seabed level. It is then followed by downward extrapolation of the up- and down-going data and a 2D deconvolution-based imaging condition. While this technique is computationally efficient, the produced image would contains crosstalk artifacts. Different orders of surface-related multiples reflection are not separated in the up-going and down-going data. As a results, when the up-going data is downward extrapolated into the up-going wavefield, there are energy within the wavefield that is associated the primary and higher-order surface-related reflections.

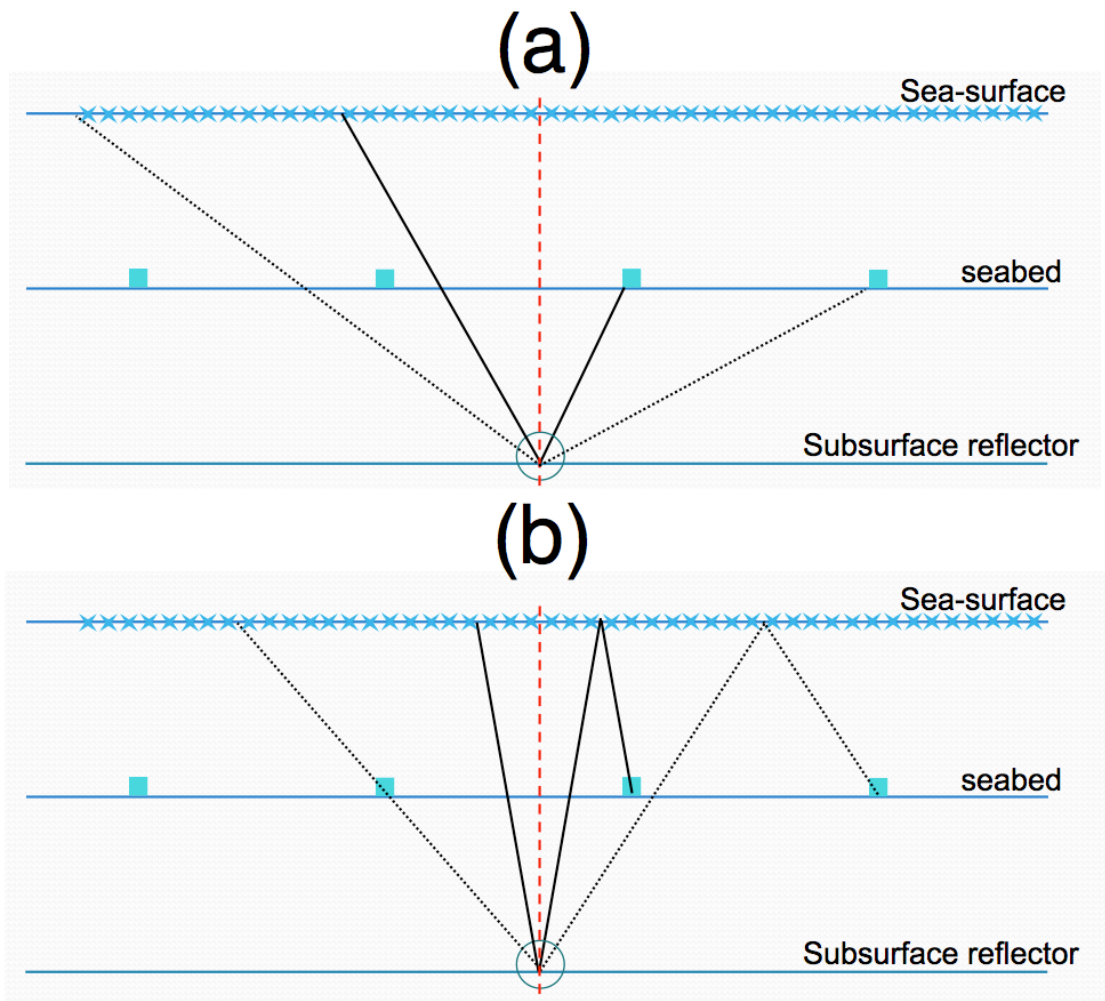


Figure 2.2: (a) shows the reflection angle ( $\theta_1$ ) by the primary reflection and (b) shows the reflection angle ( $\theta_2$ ) by the mirror reflection at the same sub-surface image location for ocean bottom node acquisition geometry. Notice that the reflection angles are different between the primary and the mirror signals. [NR] chap2/. primir

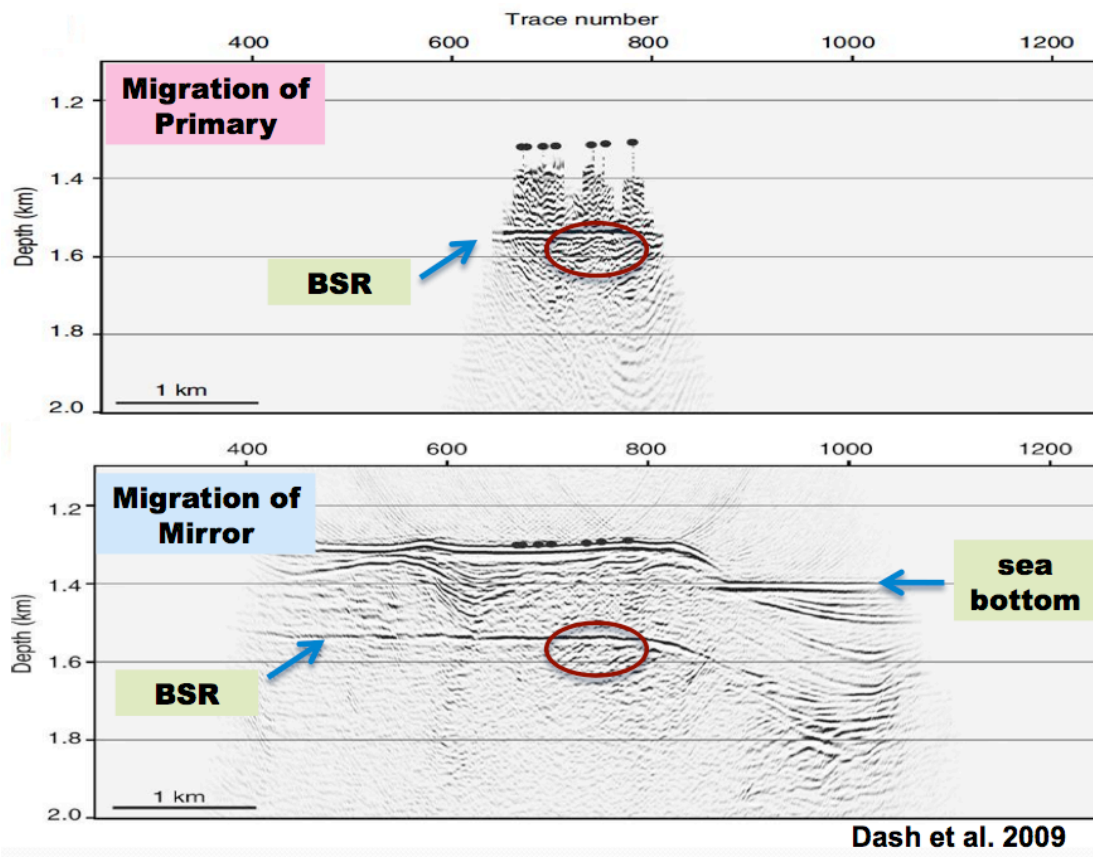


Figure 2.3: Kirchhoff migration of ocean bottom dataset using (a) the primary data and (b) the multiple data. This figure is extracted from Dash et al. (2009). [NR] chap2/. DashRTM

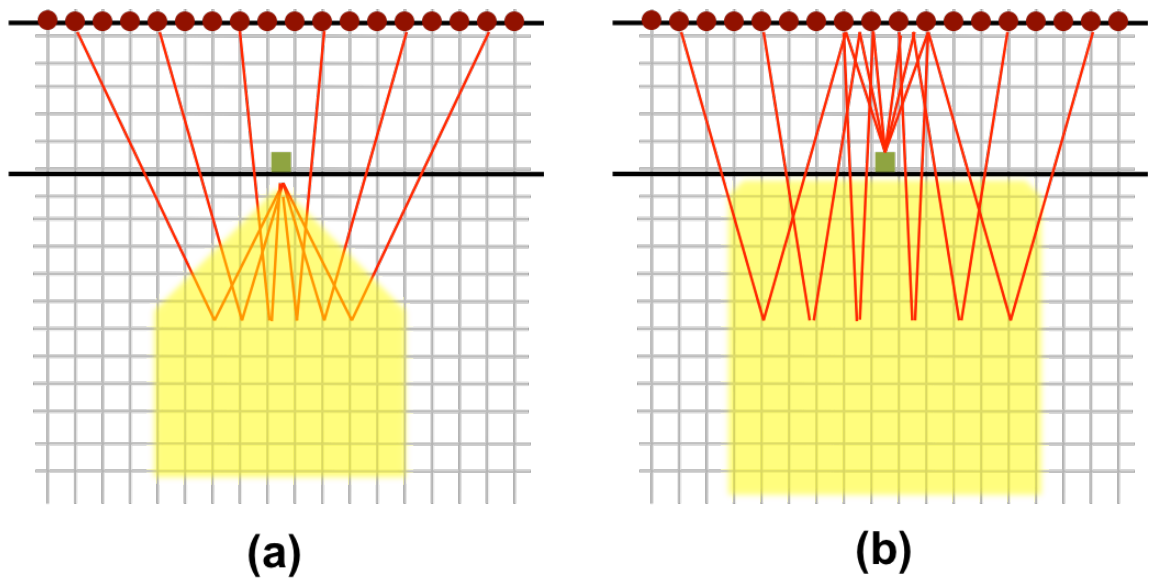


Figure 2.4: The relative illumination area (highlighted in yellow) of the (a) primary and (b) mirror events for ocean-bottom node geometry. Six rays with the same source and receiver pairs are shown. The ray diagram suggests that for the same set of rays, the primary reflection has a higher image space sampling. [NR]

chap2/. illumupdown

Likewise for the down-going wavefield. In the traditional cross-correlation imaging condition, the up-going wavefield and the down-going wavefield are correlated. There will be energy from the up-going wavefield and energy from the down-going wavefield that are not associated with the same order of reflections, which results in crosstalk noise in the image. Although deconvolution-based imaging condition can alleviate this problem, the mechanism that generates these artifacts still exists in the imaging condition. In contrast to Muijs' method, joint inversion can optimally combine structural information provided by two types of reflections that are free from crosstalk.

In this chapter, I will focus on the joint inversion of the acoustic (P) wave signal. First, I will discuss the data-domain least-squares reverse-time migration method. Next, I will apply the inversion scheme to a 2D synthetic SEAM model and the 2D Cascadia ocean-bottom field dataset and show the overall improvement of the joint inversion result. In chapters 3, I will show the application of these methods to a 3D field data example.

## SEISMIC IMAGING BY LEAST-SQUARES REVERSE-TIME MIGRATION (LSRTM)

Least-squares migration (LSM) (Cole and Karrenbach, 1992; Ji, 1992a; Lambare et al., 1992; Nemeth et al., 1999) poses the imaging problem as an linearized inversion problem. The Born forward modeling operator in LSM is obtained by linearizing the wave equation with respect to the image model. Many authors (Ji, 1992b; Wong et al., 2011) has pointed out that the Born modeling operator is the adjoint of the migration operator used in imaging. If we think of the adjoint operation as an approximation to the inverse operation, then migration provide an approximate solution to the LSM inverse problem. The goal of LSM is to obtain a more accurate solution than traditional imaging by enforcing the consistency between the synthetic and observed data. Least-squares reverse-time migration (LSRTM) is a class of least-squares migration that uses two-way wave propagation. I will explain LSRTM by first introducing the reverse-time migration (RTM) operator. Afterward, I will introduce the Born forward

modeling as the adjoint to RTM and how they are represented in the LSM objective function.

In reverse-time migration, the image is produced by multiplying the forward modeled source wavefield,  $U_o(\mathbf{x}, \mathbf{x}_s, t)$ , with the reverse-time extrapolated receiver wavefield,  $U_r(\mathbf{x}, \mathbf{x}_r, t)$ , at every time-step,

$$\mathbf{m}_{mig}(\mathbf{x}) = \sum_{\mathbf{x}_r, \mathbf{x}_s, t} U_o(\mathbf{x}, \mathbf{x}_s, t) U_r(\mathbf{x}, \mathbf{x}_r, t; \mathbf{x}_s), \quad (2.1)$$

where  $t$  is time,  $m(\mathbf{x})$  represents the structural image at subsurface location  $\mathbf{x}$ .  $\mathbf{x}_s$  represents the source location and  $\mathbf{x}_r$  represents the receiver location.  $U_o(\mathbf{x}, \mathbf{x}_s, t)$  and  $U_r(\mathbf{x}, \mathbf{x}_r, t; \mathbf{x}_s)$  are solutions to the two-way acoustic constant density equation. The source and receiver wavefields satisfy,

$$\left( s_o^2(\mathbf{x}) \frac{\partial^2}{\partial t^2} - \nabla^2 \right) U_o(\mathbf{x}, \mathbf{x}_s, t) = f_s(t) \delta(\mathbf{x} - \mathbf{x}_s), \quad (2.2)$$

$$\left( s_o^2(\mathbf{x}) \frac{\partial^2}{\partial t^2} - \nabla^2 \right) U_r(\mathbf{x}, \mathbf{x}_r, t; \mathbf{x}_s) = d_{obs}(\mathbf{x}_r, t; \mathbf{x}_s), \quad (2.3)$$

where  $s_o(\mathbf{x})$  is the slowness,  $f_s(t)$  is the source signature, and  $d_{obs}(\mathbf{x}_r, t)$  is the observed data. The source and receiver wavefields are calculated using a finite-difference time domain method. For the receiver wavefield, the solution is calculated backward in time. To obtain a better image, we can go beyond migration by posing the imaging problem as an inversion problem. The solution  $m_{inv}(\mathbf{x})$  is obtained by minimizing the objective function,  $S(\mathbf{m})$ .

$$S(\mathbf{m}) = \| \mathbf{d}_{mod} - \mathbf{d}_{obs} \|^2 = \| \mathbf{d}_o + \mathbf{d}_{born} - \mathbf{d}_{obs} \|^2. \quad (2.4)$$

$S(\mathbf{m})$  measures the least-squares norm of the difference between the forward modeled data,  $\mathbf{d}_{mod}$ , and the recorded data,  $\mathbf{d}_{obs}$ . Notice that in linearizing the wave-equation, the forward modeled data,  $\mathbf{d}_{mod}$ , is broken down into two terms.  $\mathbf{d}_o$  is the forward modeled data using the full acoustic wave equation and the background slowness,  $s_o$ , as shown in equation 2.2. It can be represented as  $\mathbf{d}_o = d_o(\mathbf{x}_r, t; \mathbf{x}_s) = U_o(\mathbf{x}, \mathbf{x}_s, t) \delta(\mathbf{x} -$

$\mathbf{x}_r$ ). If the background slowness is slowly varying, the  $\mathbf{d}_o$  term will be insignificant and it can be ignored in the objective function (equation 2.4). In the next chapter, I will discuss the situation when  $\mathbf{d}_o$  is significant and how to handle it in a field dataset. The second term,  $\mathbf{d}_{\text{born}}$ , is the Born approximation of the linearized acoustic wave equation. The derivations for the linearization of the acoustic wave equation and the Born modeling operator are shown in Appendix A. The expression for  $\mathbf{d}_{\text{born}}$  is,

$$d_{\text{born}}(\mathbf{x}_r, \mathbf{x}_s, \omega) = \delta U(\mathbf{x}, t; \mathbf{x}_s) \delta(\mathbf{x} - \mathbf{x}_r), \quad (2.5)$$

where  $\delta U(\mathbf{x}, t; \mathbf{x}_s)$  represents the perturbed wavefield that is the solution to the following equation,

$$\left( s_o^2(\mathbf{x}) \frac{\partial^2}{\partial t^2} - \nabla^2 \right) \delta U(\mathbf{x}, \mathbf{x}_s, t) = -m(\mathbf{x}) \frac{\partial^2}{\partial t^2} U_o(\mathbf{x}, \mathbf{x}_s, t). \quad (2.6)$$

Notice that the force term in equation 2.6,  $(-m(\mathbf{x}) \frac{\partial^2}{\partial t^2} U_o(\mathbf{x}, \mathbf{x}_s, t))$ , is a product of the source-side wavefield and the image model defined earlier. A common way to represents the Born modeling transformation is by introducing a linear operator  $\mathbf{L}$ .

$$\mathbf{d}_{\text{born}} = \mathbf{L} \mathbf{m} \quad (2.7)$$

Note that the Born modeling operator,  $\mathbf{L}$ , is the adjoint of the reverse-time migration operator,  $\mathbf{L}^T$ .

$$\mathbf{m}_{\text{mig}} = \mathbf{L}^T \mathbf{d}_{\text{obs}} \quad (2.8)$$

The goal of least-squares migration is to invert for the model indirectly using the conjugate gradient method.

## The meaning of the least-squares migration model parameter

The output of least-squares migration can be used in reflectivity analysis. For the derivation of the equations in this section, I will direct the reader to Appendix B and

its references. At normal incidence, the LSM model parameter is,

$$m(\mathbf{x}) = \frac{2}{v_o^2(\mathbf{x})} \left( \frac{\delta v(\mathbf{x})}{v_o(\mathbf{x})} + \frac{\delta \rho(\mathbf{x})}{\rho_o(\mathbf{x})} \right), \quad (2.9)$$

where  $v_o$  and  $\rho_o$  are the migration velocity and density, respectively.  $\delta v$  and  $\delta \rho$  are the perturbation velocity and density. We can think of the perturbation velocity as deviation between the migration velocity and the true velocity. Likewise for the perturbation density. When compared to the reflectivity expression, the LSM model parameter and the reflectivity,  $R(\mathbf{x})$  are related as follow,

$$\begin{aligned} R(\mathbf{x}) &= \frac{1}{4} v_o^2(\mathbf{x}) m(\mathbf{x}), \\ &= \left( \frac{v_o(\mathbf{x})}{2} \right)^2 m(\mathbf{x}) \end{aligned} \quad (2.10)$$

Equation 2.10 suggests that we can scale the LSM output by the square of half of the background velocity to obtain the reflectivity at normal incidence.

## Joint inversion of up/down-going P wave

Joint inversion of up- and down-going signals for ocean-bottom data can potentially be a better imaging technique than migrating either signal alone, because it combines information from both sets of signals. Ocean-bottom data are first separated into acoustic up- and down-going components above the seabed. The decomposed signals are then inverted to yield one optimally combined reflectivity image. The fitting goal for such an inversion is:

$$0 \approx \begin{bmatrix} \mathbf{L}_\uparrow \\ \mathbf{L}_\downarrow \end{bmatrix} \mathbf{m} - \begin{bmatrix} \mathbf{d}_\uparrow \\ \mathbf{d}_\downarrow \end{bmatrix}, \quad (2.11)$$

where  $\mathbf{L}_\uparrow$  and  $\mathbf{L}_\downarrow$  are modeling operators that produce up-going data,  $\mathbf{d}_\uparrow$ , and down-going data,  $\mathbf{d}_\downarrow$ , from the model space ( $\mathbf{m}$ ). I use the adjoint of the acoustic reverse time migration (RTM) operator to formulate  $\mathbf{L}_\uparrow$  and  $\mathbf{L}_\downarrow$ . Two modified computational

grids are used to forward model the lowest order of up- and down-going signals, namely the primary and the receiver ghost. The formulation of the modeling and its adjoint (RTM) operator is summarized in Figures 2.5 and 2.6.

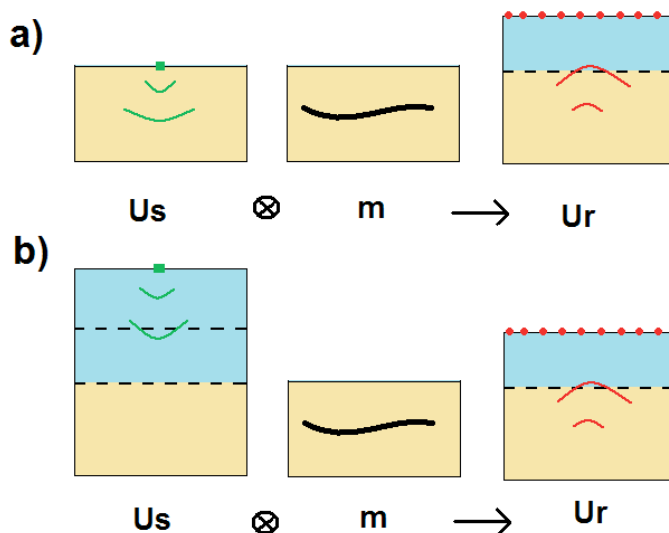


Figure 2.5: Forward modeling of (a) primary-only and (b) mirror-only data. The algorithm involves cross-correlating the source wavefield ( $U_o$ ) with the reflectivity model ( $m$ ) to generate the receiver wavefield ( $U_r$ ). Reciprocity is used here where the data, in common-receiver domain, are injected at the source location while the source wavelet is injected at the receiver location. Cross-correlation is done only with grid points below the seabed. [NR] chap2/. forward

In the modified computational grid (Figure 2.5), the primary signal is obtained by the cross-correlation of the source wavefields with the reflectivity estimate. For the down-going receiver ghost, the receiver nodes are placed at twice the water depth, which effectively represents a reflection off the sea-surface.

## COMPUTATIONAL COST OF LSRTM VS RTM

LSRTM is a computationally expensive algorithm. If an iterative inversion such as the conjugate gradient method is used, the computational cost is  $2N_{\text{iter}}$  that of regular RTM.  $N_{\text{iter}}$  is the number of iterations in the conjugate gradient. However, there are

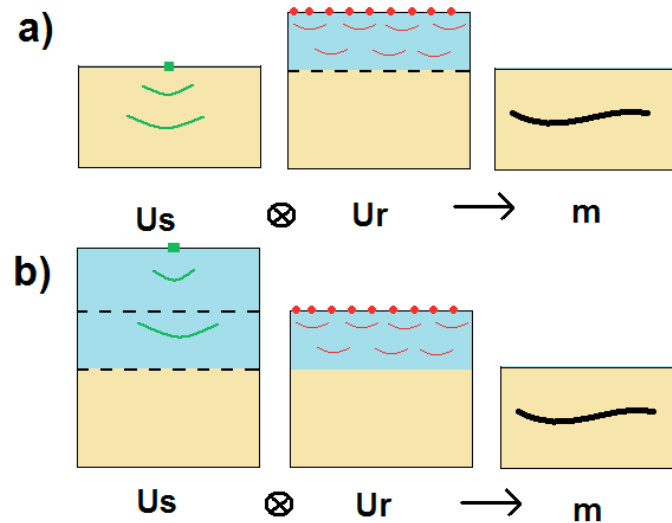


Figure 2.6: RTM of (a) primary-only and (b) mirror-only data. The algorithm involves cross-correlating the source wave field ( $U_o$ ) with the receiver wave field ( $U_r$ ) to generate the reflectivity model ( $m$ ). Cross-correlation is done only with grid points below the seabed. [NR] `chap2/. reverse`

many ways to make the algorithm more affordable. Morton and Ober (1998); Romero et al. (2000); Leader and Almomin (2012) discuss using phase-encoding to effectively reduce the computational cost of many shots into a single shot. If graphical processing unit (GPU) hardware is available, time-domain finite difference computation time can be significantly reduced (Leader and Clapp, 2013). Sometimes, the acquisition geometry can also make the cost of LSRTM more affordable. There are substantially more shots than receivers in an OBN dataset. Instead of performing each prestack depth migration based on shot gather, it is often performed by the common receiver gather.

## NUMERICAL EXAMPLE

Next, I will demonstrate the joint inversion of primary and mirror signals using a 2D synthetic example from a modified version of the SEAM model (Pangman, 2007).

Synthetic data are generated using an ocean bottom node-like geometry. Figure 2.8c shows the velocity model used for this example. The model is 4650 m deep and 12 km wide with a spacing of 15 m. The seabed is between 800 and 900 m deep.

For the synthetic data, I used the two-way acoustic wave equation to generate primary and mirror ocean bottom node data. Four-hundred shots extend from 0 to 12000 m along the sea surface at an intervals of 30 m. The receiver geometry consists of a receiver spacing of 105 m with 19 ocean bottom nodes located between 4995 m and 6900 m. Because reciprocity is used later, this geometry is equivalent to having 19 shots at the sea-bottom and 400 receivers at the sea-surface.

Typically, in an ocean bottom node dataset, the pressure and the vertical particle velocity are measured. Up- and down-going data can be extracted from PZ summation. In field data settings, imperfect separation between the up-going and down-going signal can happen. To simulate this situation, I purposely leave 20 percent of the down-going energy in the up-going data and vice versa. Figure 2.7 shows an up-going common receiver gather with and without imperfect up-down separation. We can see the mirror reflection energy arriving at around  $t = 4s$ . Because I used two-way wave equation modeling, there are also internal multiples in the data.

To compare conventional primary migration, mirror imaging, and joint inversion, I will first present the results of RTM on the conventional primary signal and the mirror signal. The corresponding image will then be compared to the joint inversion result using both signals.

### Reverse time migration on conventional primary and mirror signals

In this section, I define the term primary-RTM ( $\mathbf{m}_\uparrow$ ) to be applying the adjoint of  $\mathbf{L}_\uparrow$  to the up-going data. The term mirror-RTM ( $\mathbf{m}_\downarrow$ ) is defined similarly. In equation form, this is written as:

$$\begin{aligned}\mathbf{m}_\uparrow &= \mathbf{L}'_\uparrow \mathbf{d}_\uparrow^{mod}, \\ \mathbf{m}_\downarrow &= \mathbf{L}'_\downarrow \mathbf{d}_\downarrow^{mod}.\end{aligned}\tag{2.12}$$

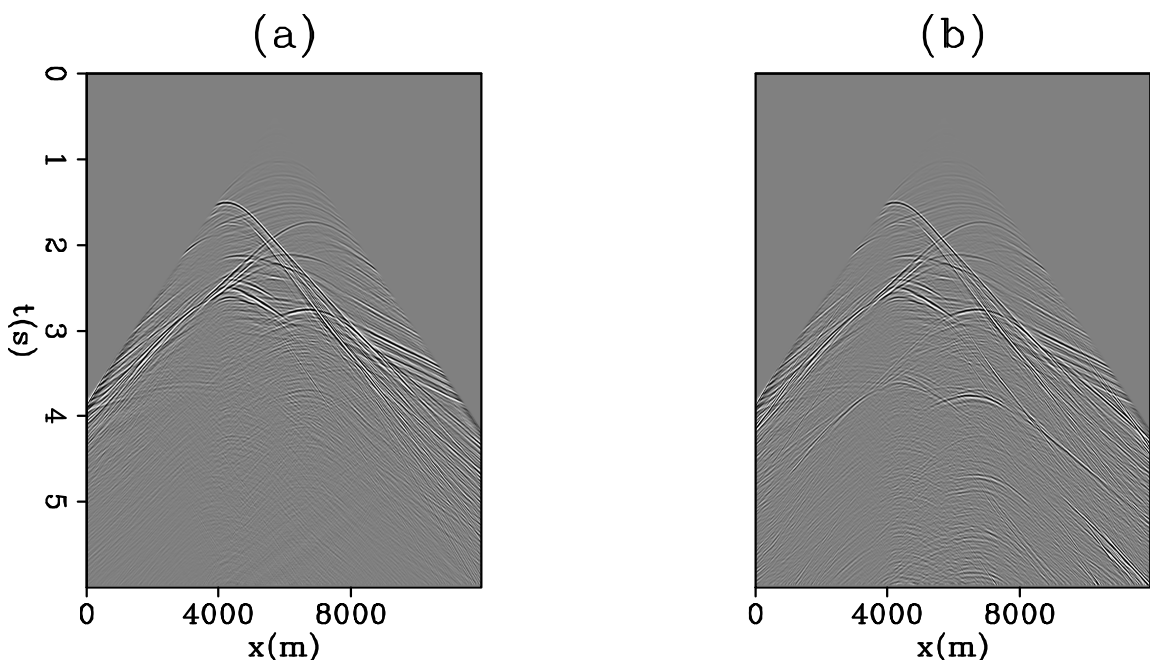


Figure 2.7: A common-receiver gather taken at  $x=5835$  m: (a) only up-going energy is present in this gather and (b) with 20 percents of down-going energy remaining in the gather. The figure is displayed with a `tpow` setting of 3 to highlight the mirror signal noise. Direct arrival and refraction energy are muted. [CR] `chap2/. modData`

Figures 2.8 b and c show the corresponding primary-RTM and mirror-RTM images. The mirror image has wider illumination than the primary image. The benefit of the wider aperture is directly correlated with the depth of the sea-bottom. The deeper the sea-bottom, the wider the illumination. The extent between the source and receiver spread also plays a role in the illumination aperture. If the spread of the source position is laterally much wider than the spread of the ocean-bottom receivers, the mirror image will illuminate a much wider area than the primary image. By comparing the two images, against the velocity model (Figure 2.8a), we can see some of the crosstalk noise as a result of imperfect up-down separation and internal multiples. The crosstalk noise can be represented in the following form,

$$\begin{aligned} \mathbf{m}_{mig} &= \mathbf{L}'_{\uparrow}(\mathbf{d}_{\uparrow} + \alpha\mathbf{d}_{\downarrow}), & (2.13) \\ &= \mathbf{L}'_{\uparrow}\mathbf{d}_{\uparrow} + \mathbf{L}'_{\uparrow}\alpha\mathbf{d}_{\downarrow}, \\ &= \mathbf{m}_{signal} + \mathbf{m}_{crosstalk}. & (2.14) \end{aligned}$$

where  $\mathbf{m}_{signal}$  represents the part of the image that carries the true signal while  $\mathbf{m}_{crosstalk}$  represents the part of the image that is the result of migrating the down-going data ( $\alpha\mathbf{d}_{\downarrow}$ ) with the primary kinematics. The crosstalk noise in the primary-RTM appears in the deeper part of the image. On the other hand, the crosstalk noise in the mirror-RTM appears in the shallower part of the image. In this way, the degradation from the crosstalk noise due to imperfect separation affects different parts of the migration images between the two datasets. This characteristic that is beneficial in joint imaging later on.

The primary and mirror events illuminate the same subsurface location at different reflection angles (Figure 2.2). Figure 2.9 shows the primary and mirror image when illuminated at a subsurface angle of  $-50$  degrees. The annotated circle shows the illuminated region from the mirror-RTM image that is not present in the primary-RTM image. The primary-RTM image is able to illuminate the sediment layers at a larger reflection angle than the mirror-RTM image as annotated by the pointers. Different parts of the subsurface are illuminated at different angles in the two datasets.

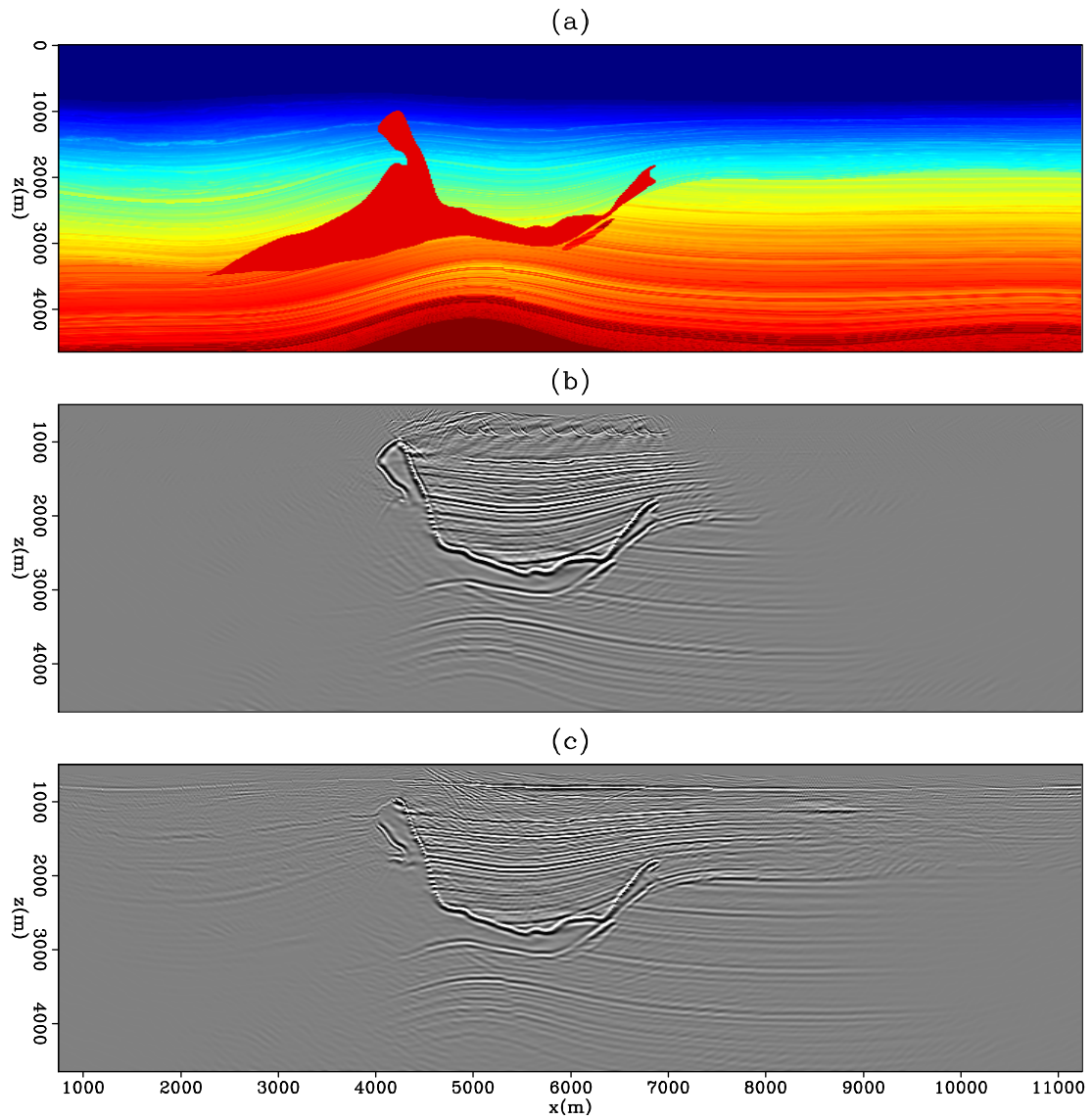


Figure 2.8: (a) The velocity model, (b) primary RTM image obtained by calculating  $\mathbf{L}'_{\uparrow} \mathbf{d}^{mod}$ , and (c) mirror RTM image obtained by calculating  $\mathbf{L}'_{\downarrow} \mathbf{d}^{mod}$ . [CR]

chap2/. rtmSap

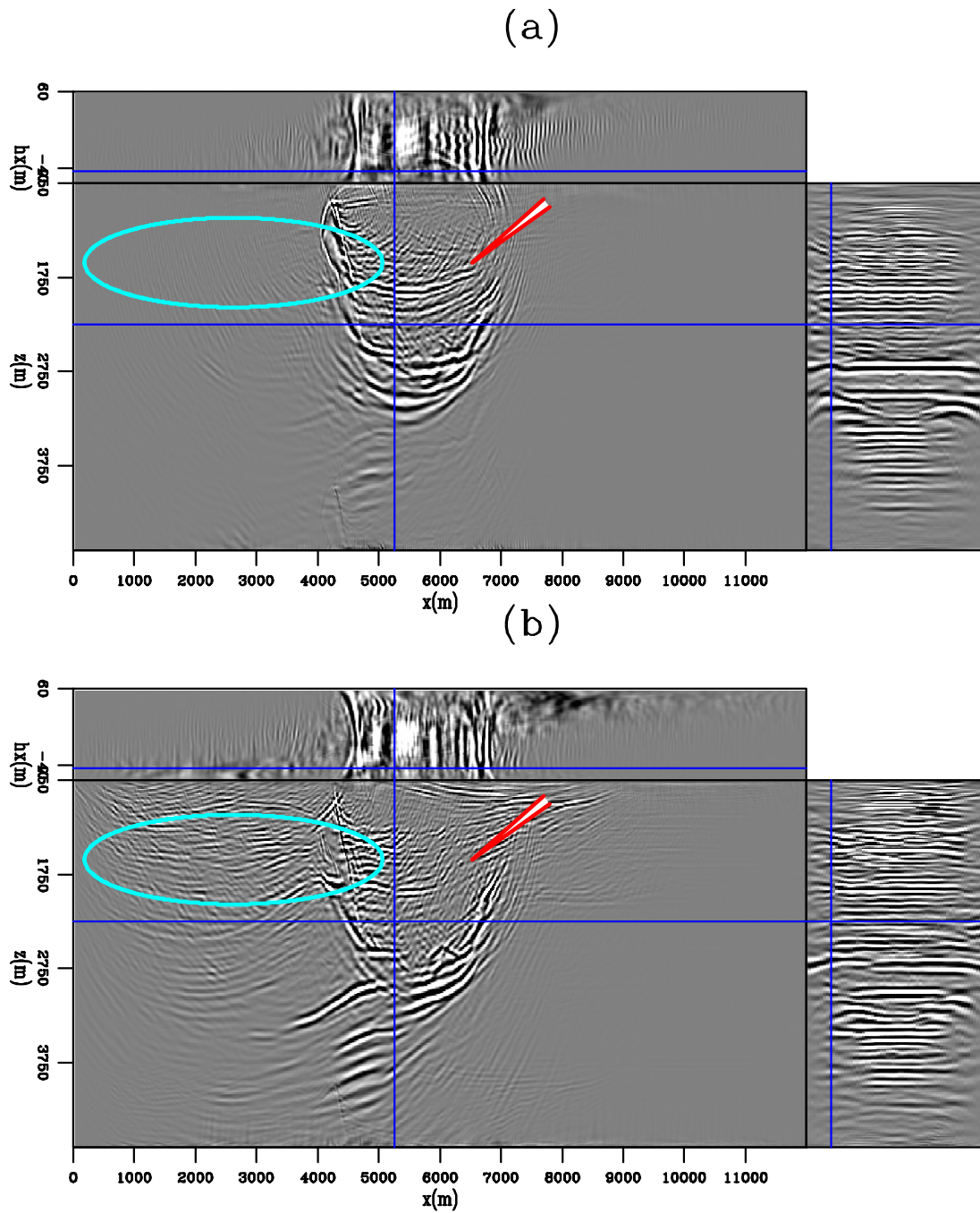


Figure 2.9: (a) Primary RTM image and (b) mirror RTM image. The front panel shows the image illuminated at a subsurface angle of -50 degrees. [CR]

chap2/. rtmSapAng

A joint image by least-squares reverse time migration could be superior to conventional mirror imaging in several ways. It will contain the wider illumination of the mirror-RTM and the illumination contribution at different subsurface angles. In addition, the crosstalk artifacts due to imperfect separation will be suppressed because these noises are not consistent between the two images.

### **Least-squares RTM Result**

A joint inversion is performed in a least-squares sense with the objective goal described in equation 2.11. Figure 2.10 shows the inversion results for the primary, the mirror, and the joint image. There is an overall improvement from the migration images in Figure 2.8b and c to the inversion image in Figure 2.10a and b, respectively. In general, the LSRTM algorithm improves the image by reducing migration artifacts, balancing the relative amplitude of the reflectors, and increasing the resolution of the image.

I have identified some areas of improvement with two close-up sections shown in Figures 2.11 and 2.12.

1. By comparing the RTM and LSRTM images in both Figure 2.11 and Figure 2.12, we can see that the overall resolution of the image is higher in the LSRTM case.
2. The annotated region A in Figure 2.11 shows a steeply dipping salt flank. It is better illuminated in the primary images than in the mirror images. The joint LSRTM image also illuminates the dipping salt flank well.
3. The annotated region B in Figure 2.11 shows a region of the sediment against a salt flank. It is better illuminated in the mirror images than in the primary images. The joint LSRTM image benefits from the mirror signal and also illuminates the sediment-salt region well.
4. Figure 2.12 shows the overall improved signal-to-noise ratio of the joint LSRTM as compared to the individual primary-LSRTM and mirror-LSRTM images above salt.

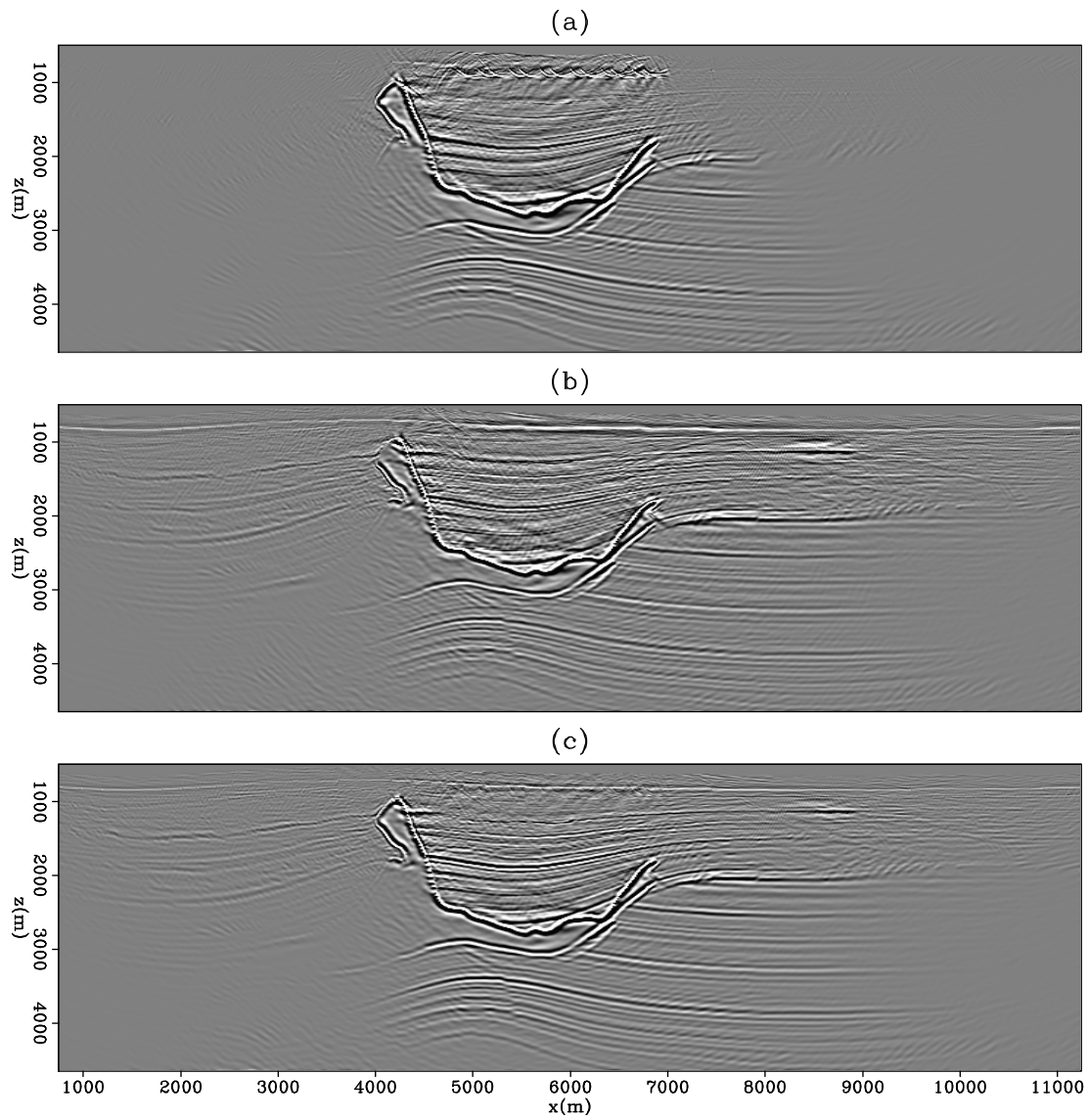


Figure 2.10: (a) Primary LSRTM image and, (b) mirror LSRTM image and (c) the joint LSRTM image. [CR] chap2/. invSap

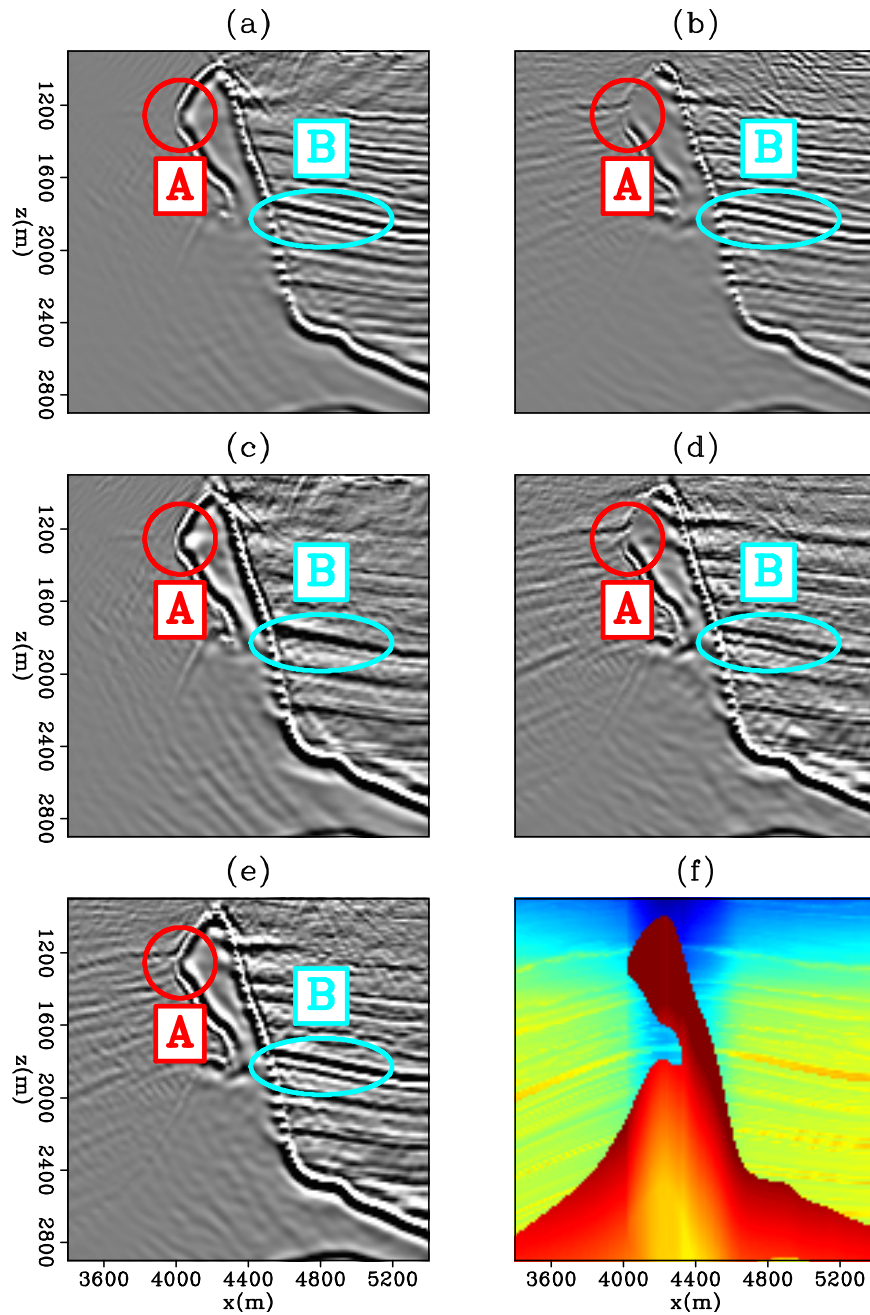


Figure 2.11: A section at  $x=3800$  to  $5800$  m and  $z=1000$  to  $3000$  m of (a) primary RTM, (b) mirror RTM, (c) primary LSRTM, (d) mirror LSRTM, (e) joint LSRTM, and (f) velocity model. [CR] `chap2/. zoomSap1v2`

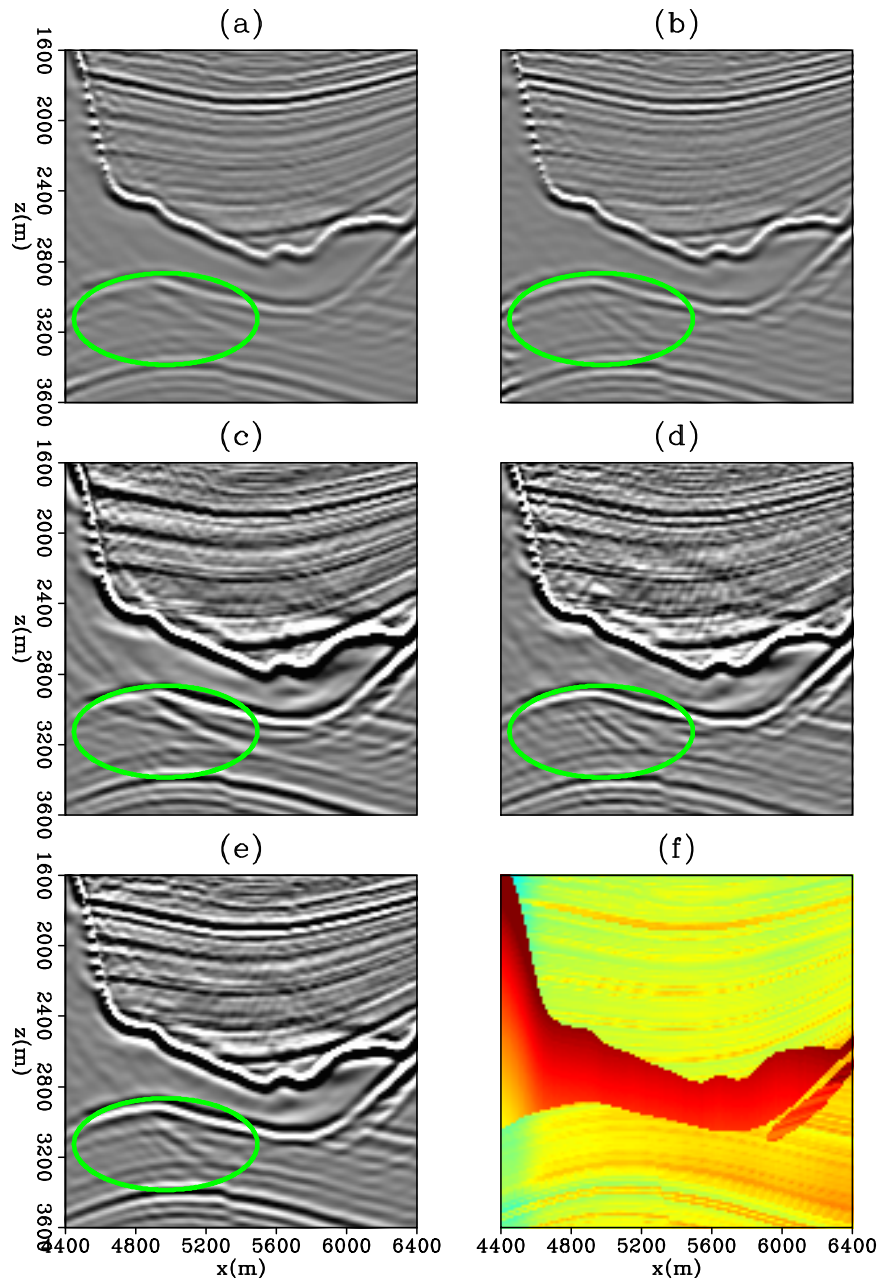


Figure 2.12: A section at  $x=4400$  to  $6400$  m and  $z=1600$  to  $3600$  m of (a) primary RTM, (b) mirror RTM, (c) primary LSRTM, (d) mirror LSRTM, (e) joint LSRTM, and (f) velocity model. [CR] chap2/. zoomSap2v2

5. The annotated region underneath the salt in Figure 2.12 also shows that the joint-LSRTM image has more continuous reflectors there with less artifacts than individual mode imaging.

This example shows that joint inversion coherently combines information from the primary and the mirror signals to produce a better illuminated and better resolved image.

## 2D FIELD EXAMPLE

Next I will present the results from applying LSRTM on an OBS survey located at the northern Cascadia continental margin offshore of western Canada. The area contains gas hydrates, which have a characteristic structure known as the bottom-simulating reflector (BSR), that marks the base of the hydrate stability zone. OBS data were collected along five parallel lines normal to the margin (Figure 2.13). Line spacing was 500 m with ten ocean-bottom seismometers deployed with 100 m spacing at a water depth of about 1300 m.

### Pre-processing

In the 2D study, I extracted a 2D shot line from directly above the OBS line. After completing the processing step described in Dash et al. (2009), I applied a gapped deconvolution with a 12-ms gap length and 300-ms filter length to suppress the source bubble. Only six of the ten OBS receivers were used for final imaging. These receivers were selected according to their data quality. Three receivers were rejected due to large tilt angles, and one receiver was rejected because it was saturated with noisy traces.

I used the adaptive decomposition method of Schalkwijk et al. (2003) to separate energy into up- and down-going wavefields. These data were bandpassed between 5 and 45 Hz to avoid dispersion in the time-domain finite-difference calculation. These data, before and after pre-processing, are shown for one common receiver gather (Figure 2.14).

A velocity model was supplied by the University of Victoria to use for imaging. Velocity values range from 1480 m/s in the water column to 1820 m/s in the sediment layer. The BSR lies at an approximate depth of 1500 m. There is a velocity inversion where the velocity value drop is going deeper across the BSR.

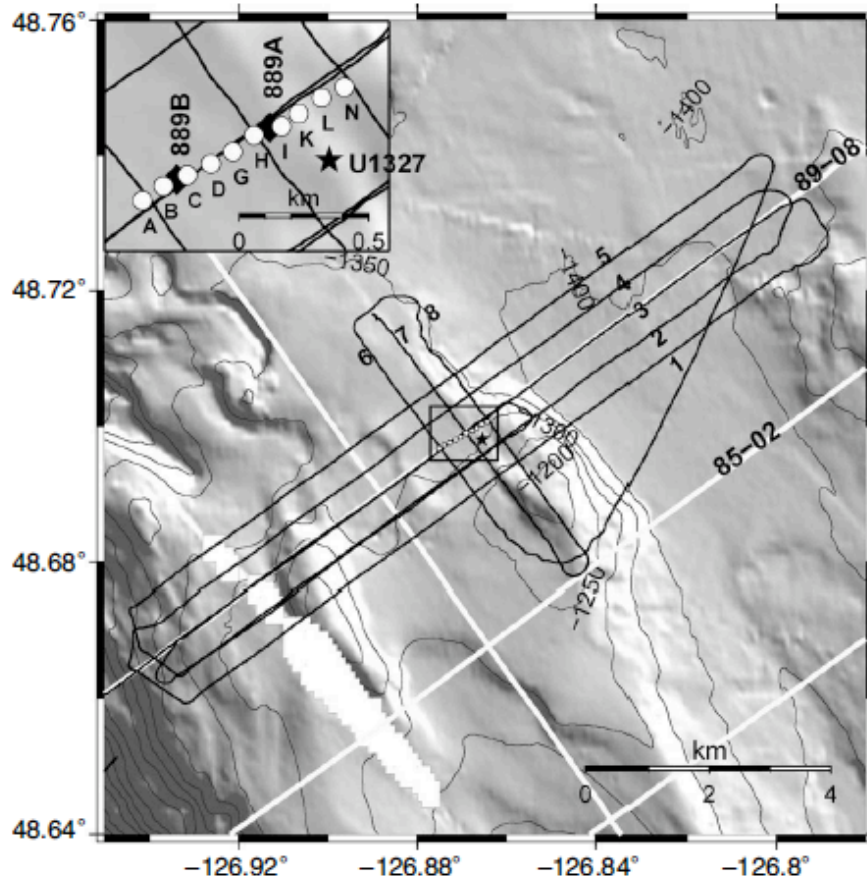


Figure 2.13: The geometry of the Northern Cascadia dataset. Ten ocean-bottom seismometers were deployed with 100 m spacing at a water depth of 1300 m. The shot line spacing was 500 m. [NR] chap2/. geo

## Conditioning of the LSRTM problem for the 2D Cascadia data

Seismic inversion is an ill-posed problem. To prevent divergence to unrealistic solutions, I added an additional term to our objective function,  $S(\mathbf{m})$ . In Nemeth et al. (1999); Ronen and Liner (2000), data weighting operators were used to remove the acquisition footprint by applying zero weighting on regions corresponding to the

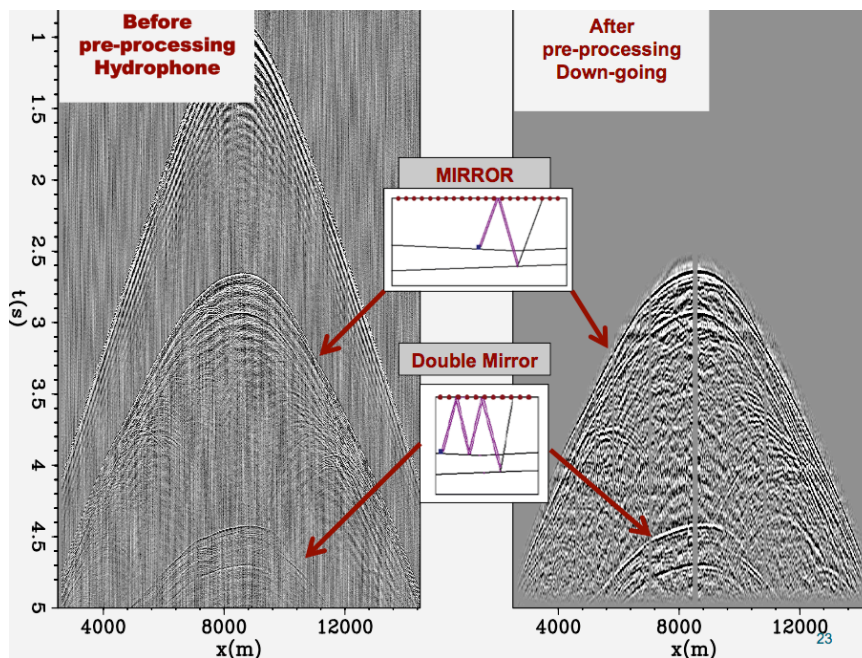


Figure 2.14: (a) A hydrophone common receiver gather (CRG) before pre-processing and (b) down-going data after pre-processing. [NR] chap2/. dataCas

acquisition gap. The overall fitting goal becomes

$$S(\mathbf{m}) = \|\mathbf{W}(\mathbf{Lm} - \mathbf{d})\|^2 + \epsilon^2 \|\mathbf{m}\|^2, \quad (2.15)$$

where  $\mathbf{W}$  is a diagonal data-weighting matrix, and  $\epsilon$  tunes the level of damping in our objective function. The criterion for choosing  $\epsilon$  is:

$$0.2 = \frac{\|\epsilon \mathbf{m}\|^2}{\|\mathbf{W}(\mathbf{L}^T(\mathbf{d}_{mod} - \mathbf{d}))\|^2}. \quad (2.16)$$

In the first iteration,  $\epsilon$  is defined by limiting the gradient contribution from the damping term to be 20% of the gradient contribution from the data fitting term. From experiments with both synthetic and field dataset, I found that this limit yields satisfactory results. For this dataset, the damping term alone seems to adequately regularize the inversion and yield a satisfactory result. Other regularization terms

are needed to further constrain the inversion for more complex survey regions.

## Migration and Inversion results

Figure 2.15a shows the primary-RTM image and Figure 2.15b shows the mirror-RTM image. I can identify some migration artifacts associated with RTM, such as several high-amplitude low-frequency artifacts. The resolution is relatively low, and the structural information below the BSR is generally difficult to identify. Similar to Figure 2.3, the primary-RTM illuminates a much smaller area compared to the mirror-RTM image. Due to the small numbers of shots, the primary-RTM also suffers from apparent edge artifacts. Figure 2.15c shows the joint-RTM, which is a simple sum of up-going and down-going signal.

I applied LSRTM for three cases as follow (1) using the up-going primary signal (primary-LSRTM), (2) using the down-going mirror signal (mirror-LSRTM), and (3) using both primary and mirror signals (joint-LSRTM). The results after 20 iterations are shown in Figure 2.16a, b, and c respectively. Overall, the inversion images have higher resolution and fewer artifacts than the RTM images. To study the benefit of joint-LSRTM, I focused on the center region where both the primary and mirror signals contribute. Figure 2.17 shows an enlarged section of the image with four different scenarios. The LSRTM results are better than the RTM results. However, when comparing the two LSRTM cases (Figures 2.17 c and d), the joint-LSRTM is far superior than the mirror-LSRTM below the BSR. An arrow highlights that a dipping reflector below the BSR is much more clearly imaged in the joint-LSRTM than in all the other scenarios.

## Discussion

Edge artifacts from the primary image have been passed onto both the joint-RTM and joint-LSRTM images. The Cascadia dataset has a shallow target area, which results in strong edge artifacts. I expect that edge artifacts will be less apparent when the target area is deeper or when more ocean-bottom nodes are included in the calculation.

The Cascadia result shows that information from the primary signal can help us to image dipping reflectors better (Figure 2.17). We can understand why better imaging of dipping reflectors is possible by observing the ray paths which illuminate a dipping reflector beneath an ocean bottom node. In Figure 2.18, the primary reflection (red) requires a shorter offset range than the mirror reflection (blue) to illuminate the target. Given that all surveys have a finite maximum offset, this translates to dipping reflectors being better imaged by the primary signal than by the mirror signal.

## CONCLUSION

While direct migration of the primary data has limited illumination aperture, direct migration of the mirror signal is less resolved in complex areas. Joint-LSRTM can image geologically complex areas with better illumination, improved resolution, and more balanced amplitude. Although only 2D modeling and migration are used, we see improvements in the joint-LSRTM image over conventional methods. Such improvements include suppression of migration artifacts, enhancement of amplitudes along true reflectors, and better resolution.

## ACKNOWLEDGMENTS

I benefited from previous work with Yaxun Tang and Gboyega Ayeni, which helped me develop methods for this chapter. I am thankful to Professor George Spence from the University of Victoria and the Dalhousie University for collection and permission

to publish the OBS data. I thank Ranjan Dash for information and previous work on the field dataset.

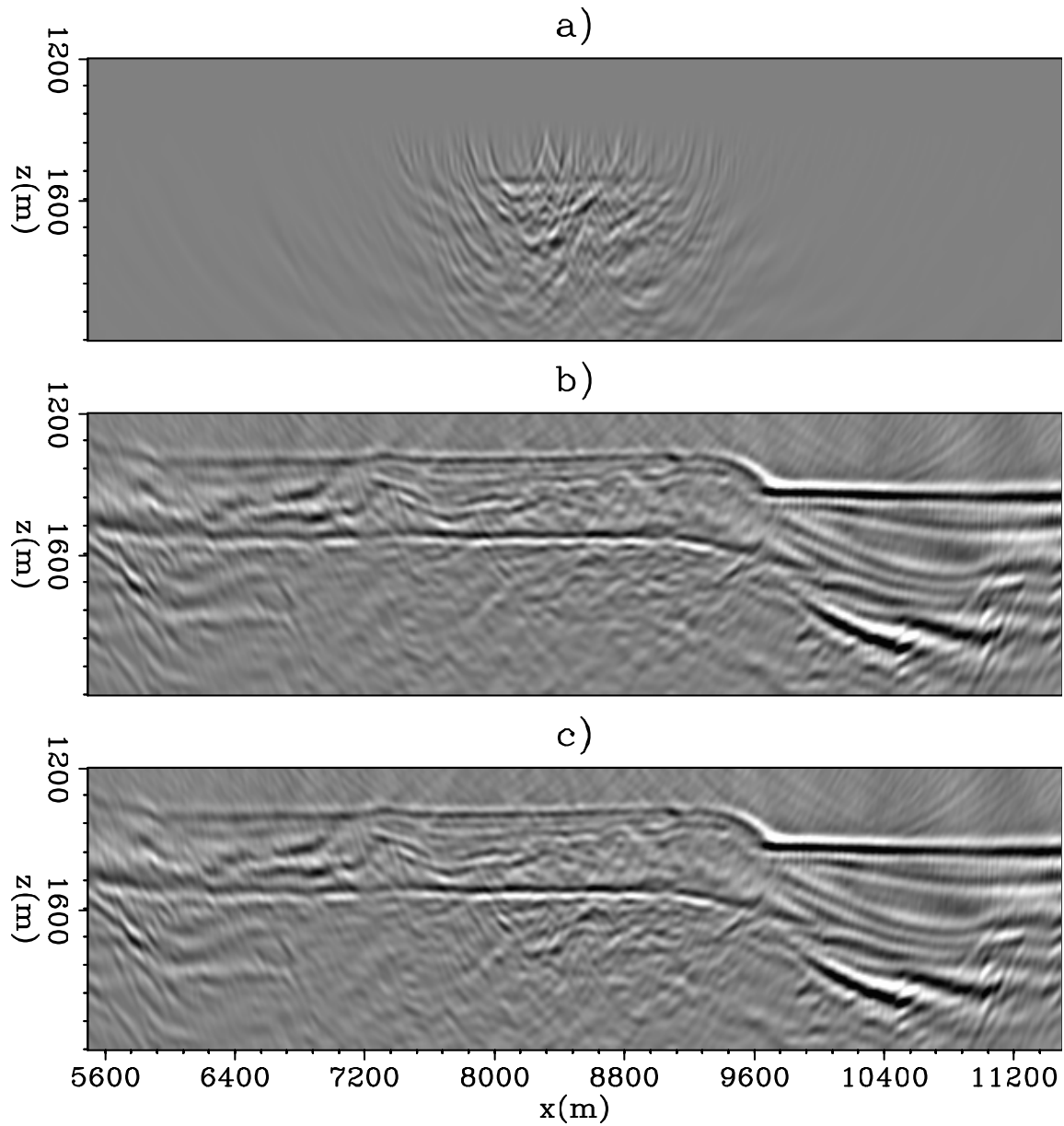


Figure 2.15: (a) the primary-RTM, (b) the mirror-RTM, and (c) the joint-RTM, which is the sum of primary- and mirror-RTM. [CR] chap2/. RTMcas

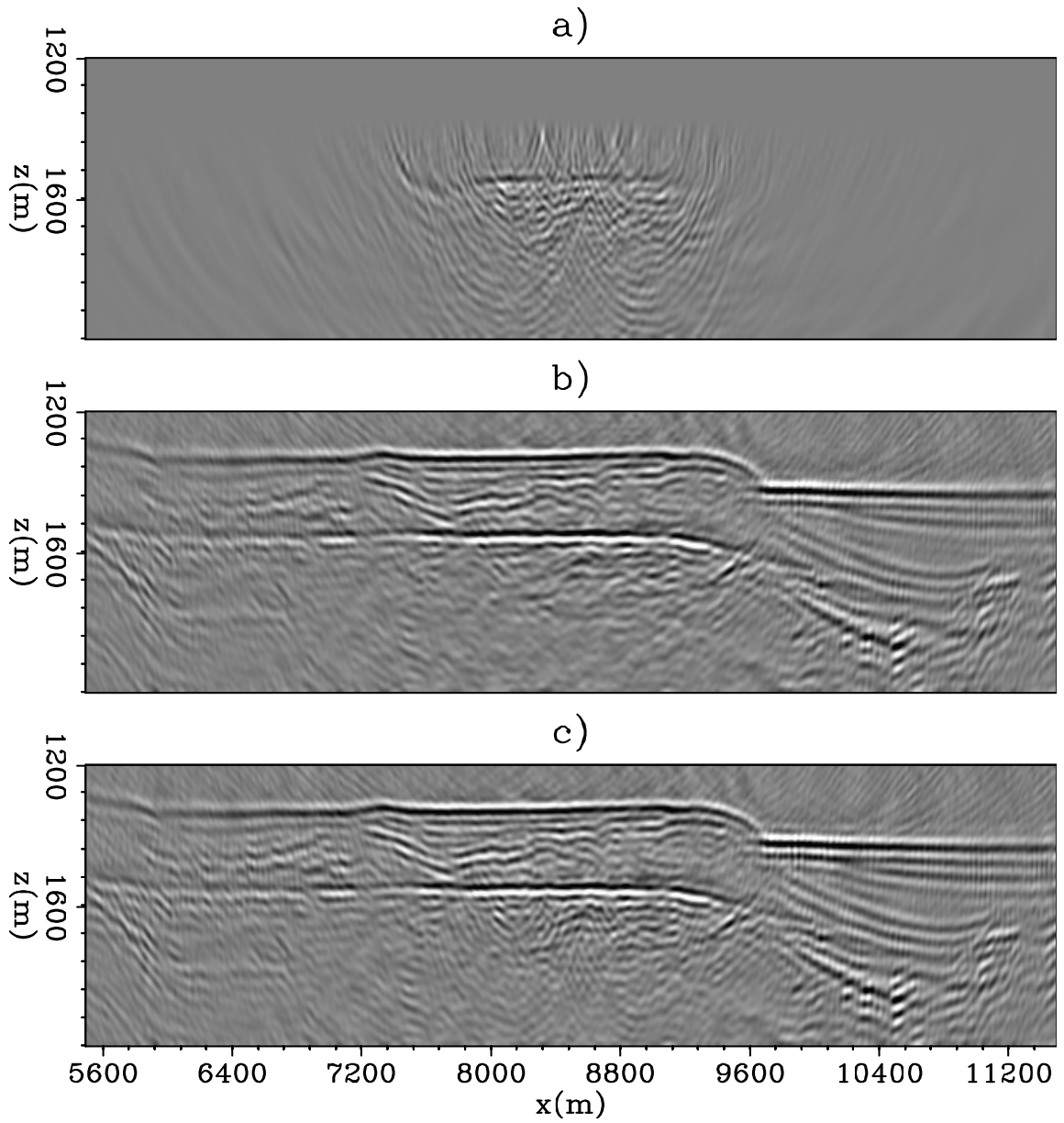


Figure 2.16: (a) LSRTM with the primary data (primary-LSRTM), (b) LSRTM with the mirror data (mirror-LSRTM), and (c) joint-LSRTM with both primary and multiple data. [CR] chap2/. LSRTMcas

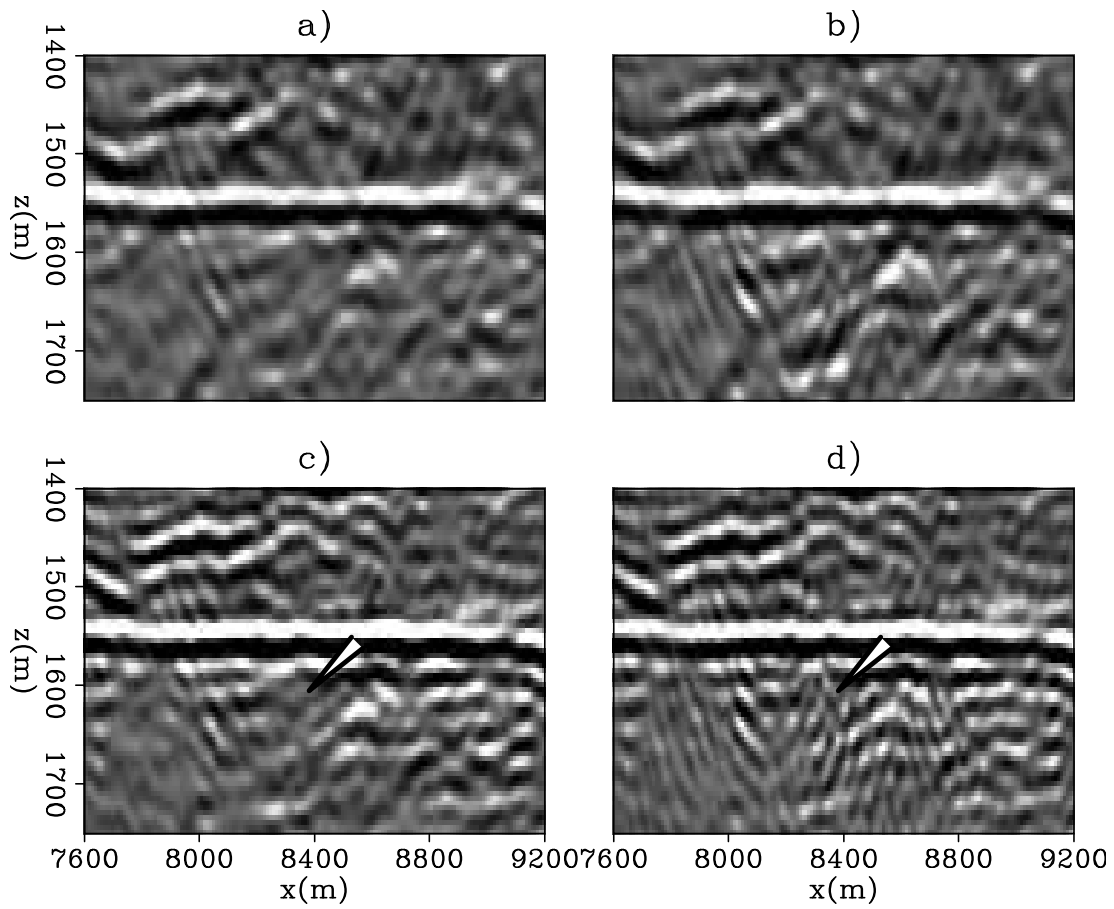


Figure 2.17: A section of the image cut from  $x=7600-9200$  m and  $z=1400-1750$  m. (a) shows the mirror-RTM, (b) joint-RTM, (c) mirror-LSRTM, and (d) joint-LSRTM.

[CR] chap2/. Zoomcas

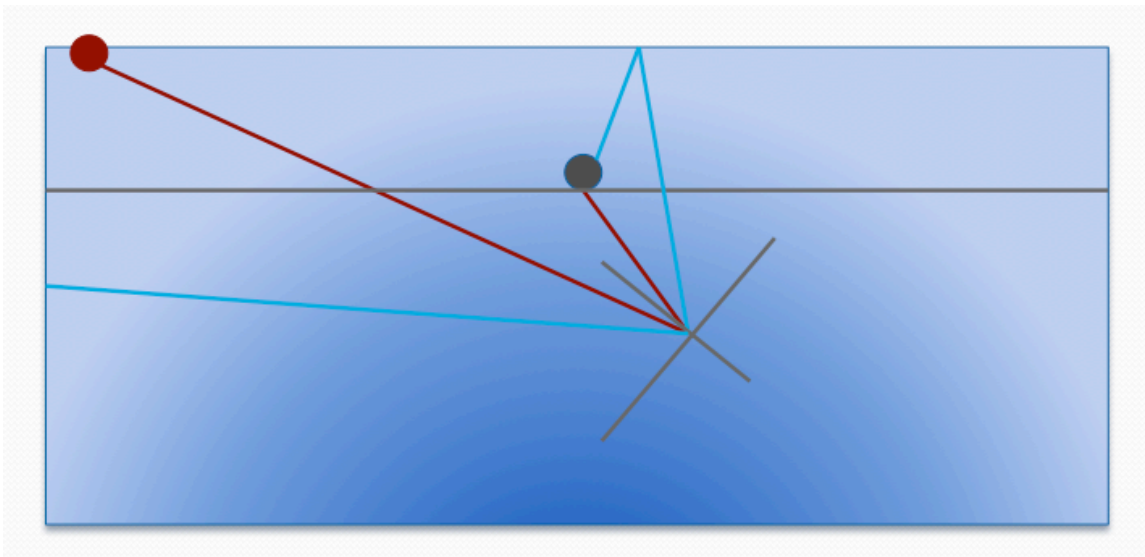


Figure 2.18: Ray paths for illuminating a dipping reflector underneath an ocean bottom node by the primary (red) and the mirror (blue) reflection. [NR]

chap2/. UpandDip

